nature energy

ARTICLES

https://doi.org/10.1038/s41560-019-0403-5

Visible-light-driven coproduction of diesel precursors and hydrogen from lignocellulose-derived methylfurans

Nengchao Luo[1,2], Tiziano Montini[3], Jian Zhang[1], Paolo Fornasiero[3], Emiliano Fonda[4], Tingting Hou[1,2], Wei Nie[1,2], Jianmin Lu[1], Junxue Liu[5], Marc Heggen[6], Long Lin[1,2], Changtong Ma[1,2], Min Wang[1], Fengtao Fan[1], Shengye Jin[5] and Feng Wang[1]*

Photocatalytic hydrogen production from biomass is a promising alternative to water splitting thanks to the oxidation half-reaction being more facile and its ability to simultaneously produce solar fuels and value-added chemicals. Here, we demonstrate the coproduction of H_2 and diesel fuel precursors from lignocellulose-derived methylfurans via acceptorless dehydrogenative C–C coupling, using a Ru-doped $ZnIn_2S_4$ catalyst and driven by visible light. With this chemistry, up to 1.04 g $g_{catalyst}^{-1} h^{-1}$ of diesel fuel precursors (~41% of which are precursors of branched-chain alkanes) are produced with selectivity higher than 96%, together with 6.0 mmol $g_{catalyst}^{-1} h^{-1}$ of H_2. Subsequent hydrodeoxygenation reactions yield the desired diesel fuels comprising straight- and branched-chain alkanes. We suggest that Ru dopants, substituted in the position of indium ions in the $ZnIn_2S_4$ matrix, improve charge separation efficiency, thereby accelerating C–H activation for the coproduction of H_2 and diesel fuel precursors.

In the search for alternatives to the use of fossil fuels, H_2 production has been the subject of intense research due to its potential as a clean energy carrier[1]. Solar-driven H_2 production over semiconductor photocatalysts in which photogenerated electrons are used to reduce protons has long been investigated as one pathway[2,3]. The process also generates holes that, if not involved in oxidizing the substrate, can oxidize the semiconductor itself under light irradiation[4], resulting in low light to hydrogen energy transformation efficiency and photocorrosion of the semiconductor[5,6]. To minimize these issues, consumption of the holes by sacrificial reagents generally accelerates the hydrogen evolution rate and prolongs the lifetime of the catalyst[7]. However, such processes produce waste and the obtained hydrogen energy sometimes cannot counteract the energy required to produce the sacrificial reagents. Therefore, employing sacrificial reagents that are easily oxidized, produced from renewable raw materials and whose oxidation products have added value is essential to solve this challenge.

Molecules present in second-generation biomass (for example, agricultural and urban organic wastes), mostly originating from photosynthesis[8], are ideal sacrificial reagents[4]. Due to the abundance and high annual yield of biomass (120 billion tonnes of total dry vegetative biomass)[9], exploiting it for H_2 production can significantly contribute to renewable energy production[10,11]. Many kinds of biomass, such as alcohols, sugars and lignocellulose, have been used to consume holes, leaving electrons to reduce protons to H_2 (refs. [12,13]), but oxidative products derived from biomass are often considered to be essentially waste. Since a variety of chemicals and fuels can be produced from biomass[14–17], it would be highly desirable to simultaneously generate H_2 using photogenerated electrons, while also utilizing the photogenerated holes to produce valuable chemicals or fuels[18]. This could help to alleviate our reliance on fossil carbon sources[19,20] and also decrease the cost of biomass-derived H_2.

In this context, lignocellulose-derived downstream products, such as 2,5-dimethylfuran (2,5-DMF) and 2-methylfuran (2-MF) are compelling candidates for the production of diesel fuels[21,22]. They can be selectively produced (>95% yields) from 5-hydroxymethylfurfural and furfural, which are produced from the abundant and easily available lignocellulose (Supplementary Fig. 1)[23–29]. In particular, the importance of 2-MF as a feedstock to provide branched-chain alkanes has been highlighted[30,31]. To produce diesel fuels from these platform molecules, the carbon chain must be lengthened to a certain degree before hydrodeoxygenation (HDO), which converts oxygenated compounds into alkanes (Fig. 1). In particular, production of branched-chain alkanes is desirable for enriching diesel fuels. Previously, chain growth has been achieved mainly by aldol condensation[32], hydroxyalkylation[31,33] and oligomerization (Supplementary Fig. 2)[34]. Among all the catalysts that promote chain growth, homogeneous acids and bases have outperformed heterogeneous ones in terms of their high activity and selectivity[31,35], but serious corrosion of the reactors and difficulty with the recycling of the catalysts has increased the cost of the diesel fuels. Thus, a green and sustainable synthetic methodology to increase the chain length would be welcome.

Here, we demonstrate the coproduction of H_2 and diesel fuel precursors (DFPs) from 2,5-DMF and 2-MF over a Ru-$ZnIn_2S_4$ photocatalyst. We show that both 2,5-DMF and 2-MF (as pure

[1]State Key Laboratory of Catalysis, Dalian National Laboratory for Clean Energy, Dalian Institute of Chemical Physics, Chinese Academy of Sciences, Dalian, China. [2]University of Chinese Academy of Sciences, Beijing, China. [3]Department of Chemical and Pharmaceutical Sciences, INSTM Research Unit, ICCOM-CNR Trieste Research Unit, University of Trieste, Trieste, Italy. [4]Synchrotron SOLEIL, Saint Aubin, Paris, France. [5]State Key Laboratory of Molecular Reaction Dynamics and Collaborative Innovation Centre of Chemistry for Energy Materials (iChEM), Dalian Institute of Chemical Physics, Chinese Academy of Sciences, Dalian, China. [6]Ernst Ruska Centre for Microscopy and Spectroscopy with Electrons and Peter Grünberg Institute, Forschungszentrum Juelich GmbH, Juelich, Germany. *e-mail: wangfeng@dicp.ac.cn

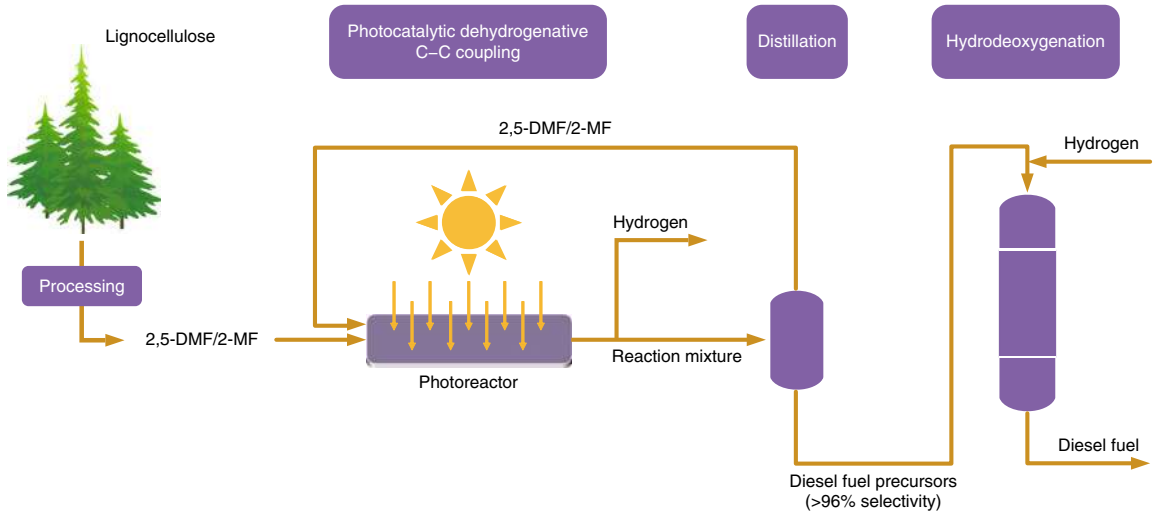

Fig. 1 | Conceptual process diagram for the production of diesel fuels from lignocellulosic waste. The diagram presents a possible process for the production of diesel fuels from second generation biomass. Methylfurans can be obtained by chemical processing of lignocellulosic wastes and oligomerized, forming oxygenated compounds in the C_{10}–C_{20} range. These DFPs can be easily separated from unreacted methylfurans by distillation and finally converted into hydrocarbons by HDO. The key point of this process is the oligomerization step, which could be easily performed in a photocatalytic way using the Ru-$ZnIn_2S_4$ catalyst presented in this work. The photocatalyst operates under irradiation with visible light, yielding dimers, trimers and tetramers with high selectivity and coproducing H_2, which can partially fulfil the requirement of the HDO step.

compounds or in mixture) undergo dehydrocoupling, producing oxygenated compounds with a number of carbon atoms typical of diesel fuels. After HDO, a complex mixture of alkanes, containing a large fraction of branched chains, is obtained. We suggest that Ru dopants improve charge separation efficiency, thereby accelerating C–H activation for the photocatalytic dehydrocoupling reactions with coproduction of H_2.

Catalyst characterization

The Ru-$ZnIn_2S_4$ catalyst was prepared by a one-pot hydrothermal method. The Ru content was determined to be 0.46 mol% by inductively coupled plasma atomic emission spectroscopy (ICP-AES). X-ray diffraction (XRD) patterns of pristine $ZnIn_2S_4$ and Ru-$ZnIn_2S_4$ show diffraction patterns typical of hexagonal $ZnIn_2S_4$ (Fig. 2a)[7]. Shift of the (006) reflection to a higher angle suggests Ru is incorporated into the $ZnIn_2S_4$ lattice. The Ru-$ZnIn_2S_4$ catalyst presents as nanoflowers with sheet-like wrinkles (Supplementary Fig. 3a,b). Their sizes are mostly located in the range of 0.6–1.6 µm (Supplementary Fig. 3c). High-angle annular dark-field scanning transmission electron microscopy (HAADF-STEM) images (Supplementary Fig. 3d–f) reveal the lamellar structure of Ru-$ZnIn_2S_4$. The lattice fringe of 0.33 nm in Fig. 2b is attributed to the (102) interplanar distance[8], and the thickness of the slab is ~6 unit cells in the (001) direction (Supplementary Fig. 3g)[36]. Fast Fourier transform (FFT) patterns can be interpreted from the hexagonal structure in Fig. 2b. In agreement with these results, the XRD patterns present very broad peaks for the reflections (*hkl*), with a high *l* value (Fig. 2a). An energy-dispersive X-ray (EDX) map in the STEM shows a uniform dispersion of zinc, indium and sulfur elements (Supplementary Fig. 3h). No large Ru or RuS_2 particles and clusters are observed, consistent with the XRD results.

X-ray absorption near-edge structure (XANES) and extended X-ray absorption fine structure (EXAFS) spectroscopies were carried out to characterize the local structure and the mean oxidation state of the metals present in the Ru-$ZnIn_2S_4$ material. The XANES spectra and the Fourier transformed (FT) k^3-weighted EXAFS signals at the Zn and In K edges are presented in Supplementary Fig. 4 for the Ru-$ZnIn_2S_4$ and $ZnIn_2S_4$ samples, together with the respective standard materials (ZnS and In_2S_3). The fitting results for the EXAFS signals at the Zn and In K edges are summarized in Supplementary Table 1. The local structure around the Zn ions is described by four sulfur ions, while the EXAFS signal originating from the indium ions suggests the presence of five sulfur ions, divided into two groups and showing the presence of two In–S distances. This situation is related to the fact that indium is hosted into two different sites within the crystallographic structure of $ZnIn_2S_4$: a distorted tetrahedral site and a distorted octahedral site, with the same population. As a result, an overall coordination number (CN) of around five is obtained. Notably, a slightly higher Debye–Waller factor is obtained for In–S with respect to the Zn–S case, to compensate the various In–S distances observed for the two crystallographic sites.

The XANES/EXAFS spectra acquired at the Ru K edge for the Ru-doped $ZnIn_2S_4$ sample is presented in Fig. 2c–e, together with the extracted EXAFS signal $\chi(k)$ and the magnitude of the FT signal. XANES results for Ru-doped $ZnIn_2S_4$ samples resemble those for the RuS_2 material, suggesting a comparable structural environment for Ru dopants (Fig. 2c). Notably, Ru metal originates an EXAFS signal with a completely different feature (Fig. 2d,e). The EXAFS signals of Ru-doped $ZnIn_2S_4$ were fitted to extract information about the local environment around the Ru ions (Fig. 2f and Supplementary Table 1). For the Ru-$ZnIn_2S_4$ sample, the first coordination shell around Ru is well fitted, including two contributions. The major type of neighbour, accounting for ~92 at% of Ru, agrees well with sulfur ions with CN very close to five. These results indicate that the dopant Ru mostly exists as isolated entities that are incorporated within the $ZnIn_2S_4$ lattice in a substitutional position for indium ions (substitutional Ru ions, Fig. 2f). Together with substitutional Ru ions, a minor contribution to the EXAFS signal originates from a Ru–Ru distance with very small CN and a Ru–Ru distance longer than that expected for standard Ru metal (Supplementary Table 1). This situation can be related to the formation of tiny metallic Ru clusters in which the Ru–Ru distance is elongated. A similar elongation has already been reported in the literature for very small Ru(0) nanoparticles in which the CN was much lower than that of bulk metal[37], and has also been observed for other metals, such as Pd[38].

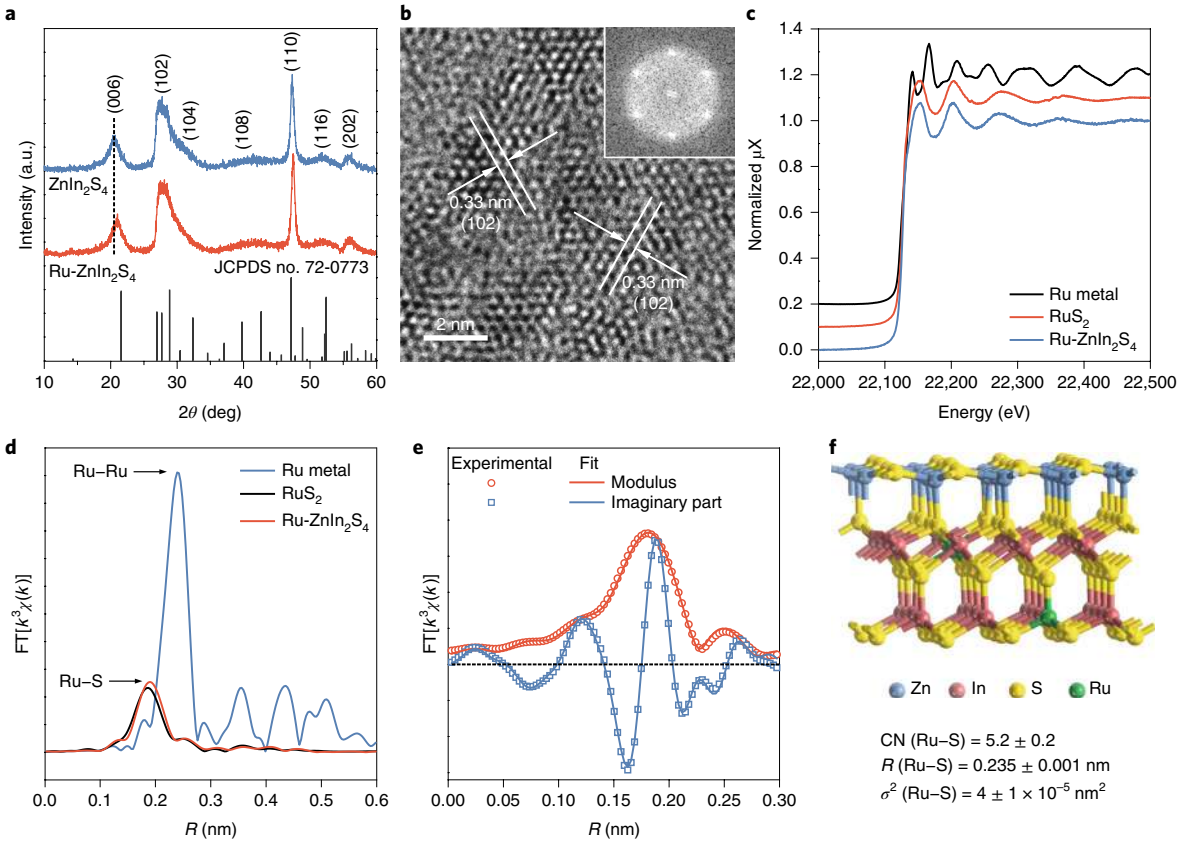

Fig. 2 | Characterization of the Ru-$ZnIn_2S_4$ photocatalyst. a, XRD patterns of Ru-$ZnIn_2S_4$ and undoped $ZnIn_2S_4$, indexed accordingly to the hexagonal $P6_3mc$ space group (JCPDS card no. 72-0773). The dashed line highlights the shift of the pattern induced by Ru doping. **b**, Representative high-resolution TEM image of Ru-$ZnIn_2S_4$, with arrows highlighting the (102) interplanar distance. Inset, the corresponding FFT of Ru-$ZnIn_2S_4$. **c**, Stacked XANES spectra of Ru-$ZnIn_2S_4$, Ru metal and RuS_2 recorded at the Ru K edge. μX is the X-ray absorption. **d**, Extracted $k^3\chi(k)$ EXAFS signals of Ru-$ZnIn_2S_4$, Ru metal and RuS_2. **e**, Fit of the FT k^3-weighted $\chi(k)$ of the EXAFS signals of Ru-$ZnIn_2S_4$ at the Ru K edge. **f**, Schematic of the Ru-$ZnIn_2S_4$ structure and the fitting results of Ru–S coordination.

Visible-light-driven coproduction of H_2 and DFPs

2,5-DMF and 2-MF are selectively obtained from processing hexosan- and pentosan-containing lignocellulose, respectively[22,29,31], and both are competitive candidates for diesel fuel production. The Ru-doped $ZnIn_2S_4$ proved to be active in catalysing the direct dehydrocoupling of 2,5-DMF and 2-MF to H_2 and DFPs under visible-light irradiation, better than other metal-doped $ZnIn_2S_4$ catalysts (Supplementary Fig. 5). The reactions are thermodynamically uphill ($\Delta G \approx 0.32$–0.34 eV, Supplementary Table 2), requiring simultaneous cleavage of the unactivated C–H bond and release of H_2 (refs. [39,40]).

Here, dehydrocoupling of 2,5-DMF yielded mainly H_2 (40.3 mmol $g_{catalyst}^{-1}$), dimers (C_{12}, 4.69 g $g_{catalyst}^{-1}$) and trimers (C_{18}, 1.84 g $g_{catalyst}^{-1}$) as products; a small amount of tetramers (C_{24}, 0.24 g $g_{catalyst}^{-1}$) was produced in 12 h (Fig. 3b and Supplementary Fig. 6a). Amounts of higher oligomers were negligible. The conversion of 2,5-DMF was 15.2% after 12 h of irradiation. The identified products involve dimeric and trimeric isomers generated because of radical resonance from furfuryl sites to furan rings (Supplementary Table 3, Supplementary Note 1 and Supplementary Fig. 7). Time profiles of trimers and tetramers show induction periods, implying that trimers and tetramers were produced from dimers in consecutive reactions. Higher oligomers were less inclined to form due to steric hindrance for C–C coupling. As a result, the selectivity of DFP decreased a little to 96% and branched-chain DFPs increased slightly to 44%; these values were maintained after 12 h of reaction (Supplementary Fig. 8a).

The production rates of H_2 and DFPs were further improved to 6.0 mmol $g_{catalyst}^{-1}$ h^{-1} and 1.04 g $g_{catalyst}^{-1}$ h^{-1}, respectively, with Ru-$Zn_2In_2S_5$ catalyst (Supplementary Fig. 5). Scaling up the reaction by 20× using Ru-$ZnIn_2S_4$ catalyst under irradiation with 86 W LEDs for 48 h afforded DFPs in 28.0 wt% isolated yield. Notably, the dehydrocoupling of 2,5-DMF over Ru-$ZnIn_2S_4$ shows an apparent quantum yield (AQY) of 15.2%, approximately twice that when over $ZnIn_2S_4$ (8.0% of AQY), implying the promotional effects of Ru dopants. The Ru-$ZnIn_2S_4$ catalyst became a bit less active within 50 h and then maintained this activity (Fig. 3c). H_2 and total liquid products were generated with the same trends, indicating electrons and holes were simultaneously consumed. After reaction for 100 h, the selectivities of DFPs and branched-chain DFPs were 97% and 43%, respectively (Fig. 3d). The Ru-$ZnIn_2S_4$ catalyst showed no significant change after reaction according to XRD, TEM and X-ray photoelectron spectroscopy (XPS) results (Supplementary Figs. 9–11).

The dehydrocoupling of 2-MF to DFPs over Ru-$ZnIn_2S_4$ shows similar trends but with a slower reaction rate (Fig. 3e and Supplementary Fig. 6b) and a lower AQY (1.9%). The branched-chain DFPs increased from 25% to 35% during 12 h of reaction (Supplementary Fig. 8b). Unlike 2,5-DMF, tetramers (C_{20}) here also have an adequate chain length to be included in DFPs, which was thus produced with 100% selectivity. Notably, in all of these reactions, weakly coloured liquids were obtained after photo-irradiation, demonstrating that uncontrollable oligomerization of the substrates is a very marginal process (Supplementary Fig. 12).

Cross-coupling of 2-MF and 2,5-DMF was conducted with a volume ratio of 3:1 as an example targeting a diesel fuel with more abundant constituents (Supplementary Fig. 6c). The identified products are presented in Supplementary Table 4. The most

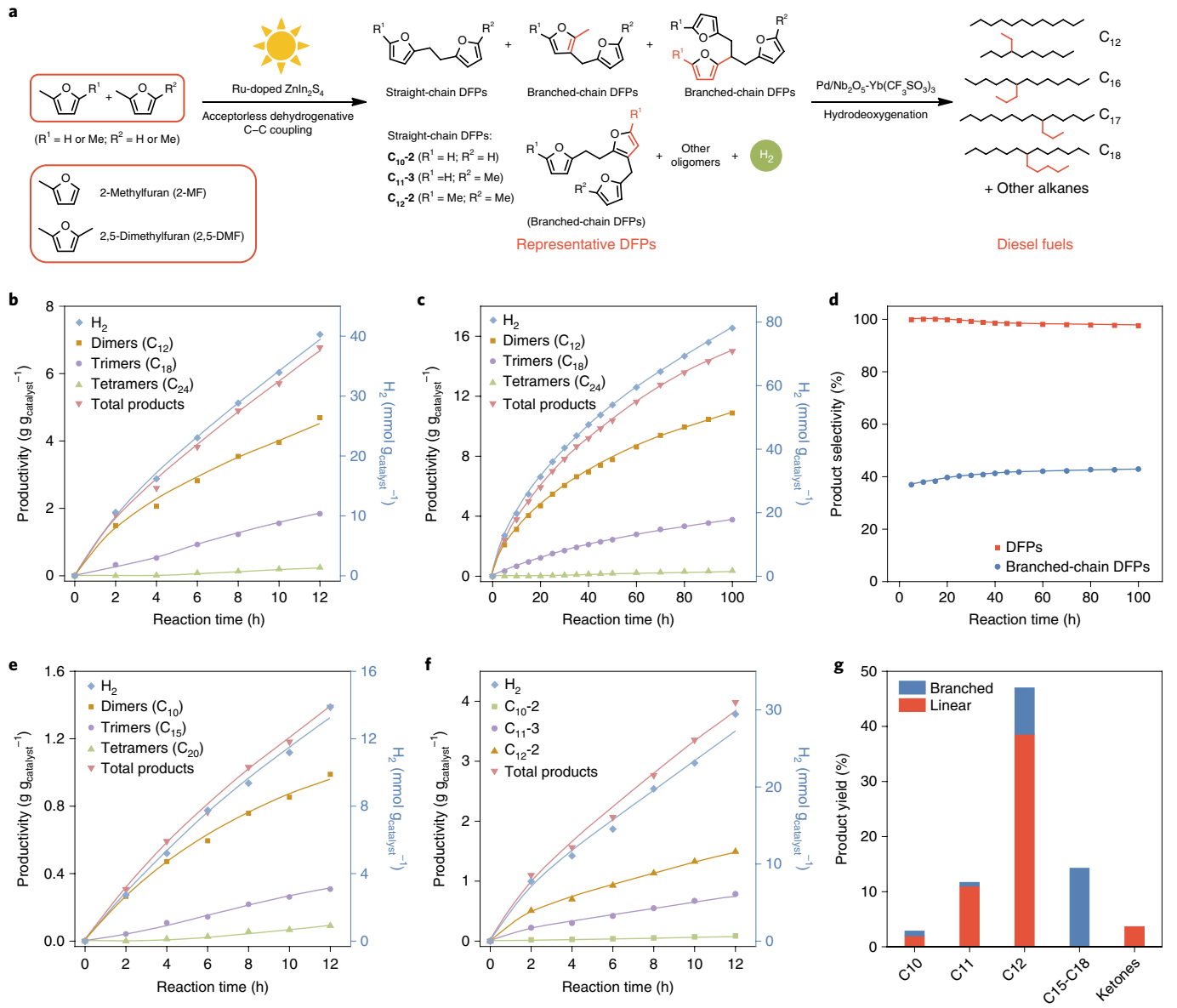

Fig. 3 | Visible-light-driven conversion of 2,5-DMF/2-MF into diesel fuel by photocatalytic dehydrocoupling followed by HDO. a, Schematic representation of the chemical reactions involved in the suggested process for conversion of 2,5-DMF/2-MF into diesel fuel. **b**–**d**, Results from photocatalytic dehydrocoupling of 2,5-DMF as substrate: standard experiment (**b**), catalyst lifetime evaluation (**c**) and selectivity to oxygenated DFPs and branched-chain DFPs (**d**). **e**, Results from photocatalytic dehydrocoupling of 2-MF during a standard experiment. **f**, Results from photocatalytic dehydrocoupling of mixture of 2,5-DMF and 2-MF (1:3 by volume) during a standard experiment. **g**, Yields of products from HDO using DFPs produced by a scaled-up photocatalytic dehydrocoupling. Total products is equal to the sum of produced dimers, trimers and tetramers. Curves drawn on top of the data are guides to the eye. Each point represents the average of at least two experiments (standard deviations were always below 10%).

abundant product was from the coupling reaction of two 2,5-DMFs through furfuryl carbon (**C_{12}-2**, 1.49 g $g_{catalyst}^{-1}$) even if the 2,5-DMF was less concentrated than 2-MF in the reaction mixture (Fig. 3f). This result is in agreement with the higher reactivity of 2,5-DMF compared to 2-MF (Fig. 3b,e). As evidence of the occurrence of the cross-coupling reaction, **C_{11}-3** (2-(2-(furan-2-yl)ethyl)-5-methylfuran) was generated with a productivity of 0.79 g $g_{catalyst}^{-1}$, together with C_{16} and C_{17} isomers (Supplementary Table 4). As expected, the dehydrocoupling of this mixture shows an AQY (6.6%) between that of 2,5-DMF and 2-MF alone.

To demonstrate the feasibility of this method to produce diesel fuels, particularly with branched-chain alkanes as constituents, a self-prepared Pd/Nb_2O_5 was initially used to screen the reaction conditions in the HDO of DFPs to alkanes (Supplementary Table 5 and Supplementary Fig. 13a–c). However, Pd/Nb_2O_5 alone afforded oxygenate intermediates with a yield of 40% in transforming DFPs obtained from the mixture of 2,5-DMF and 2-MF. To improve the selectivity of the alkanes, Lewis acid $Yb(CF_3SO_3)_3$ was used in combination with Pd/Nb_2O_5 to enhance the dehydration activity (Supplementary Table 6)[41]. Figure 3g shows the yields of products versus the number of carbon atoms. The total alkane yield is 76%, consisting of dimers and trimers (Supplementary Fig. 13d–f and Supplementary Table 4). Except *n*-dodecane and *n*-undecane, other products were mostly branched-chain alkanes, including 4-ethyldecane and C_{16}–C_{18} branched-chain alkanes, with a total yield of 24%. The formation of branched-chain alkanes demonstrates that the photocatalytic method produces branched-chain DFPs. Although we have successfully realized the coproduction of H_2 and

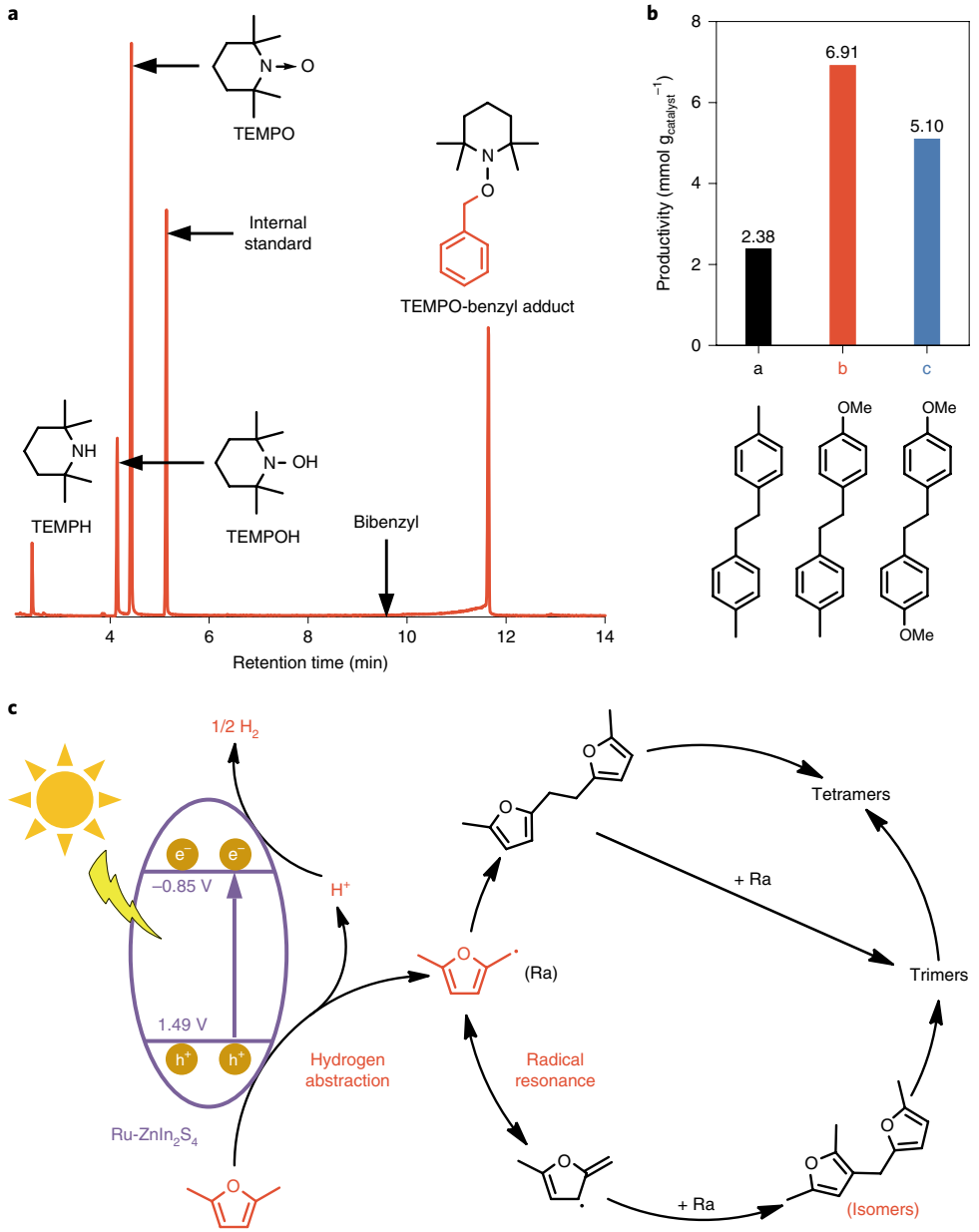

Fig. 4 | Mechanistic studies of photocatalytic acceptorless dehydrocoupling by activation of furfuryl (or benzylic) C–H bonds. a, Typical gas chromatogram of the reaction mixture after photocatalytic dehydrocoupling of toluene in the presence of TEMPO (0.2 mmol). **b**, Results from cross-coupling reaction of *p*-xylene and *p*-methyl anisole. **c**, Proposed reaction mechanism of photocatalytic dehydrocoupling of 2,5-DMF.

DFPs by photocatalysis, the yields of DFPs are lower than those of thermocatalytic processes[31].

Mechanism of dehydrocoupling of 2,5-DMF on Ru-$ZnIn_2S_4$

The reaction mechanism of photocatalytic dehydrocoupling of 2,5-DMF was studied by using toluene as a model molecule. Toluene was transformed to products similar to those of 2,5-DMF and 2-MF (Supplementary Figs. 6d and 14). However, toluene is more symmetric and has greater aromaticity, resulting in fewer kinds of products and more stable intermediates. The reaction mechanism was studied using a 2,2,6,6-tetramethylpiperidine-1-oxyl (TEMPO) trapping experiment. Addition of radical-trapping reagent TEMPO prohibited the formation of C–C coupling products (Fig. 4a), suggesting a radical mechanism[42]. The occurrence of C–H bond activation was verified by the formation of TEMPH, TEMPOH and a small amount of H_2 (0.03 mmol $g_{catalyst}^{-1}$). The formation of the TEMPO-benzyl adduct (Supplementary Fig. 15) directly indicates that the benzyl radical was formed during photo-irradiation[43]. In agreement with this, the cross-coupling reaction of *p*-xylene and *p*-methyl anisole afforded three dimers in the ratio 1:2.90:2.14 (Fig. 4b), matching $1:2m:m^2$ with m equal to 1.46 (ref. [44]). All these results agree with a radical mechanism whereby oxidizing the benzyl C–H bond by photogenerated holes gives benzylic radicals followed by their coupling. The hydrogen kinetic isotope effects (KIE) of the photocatalytic dehydrocoupling of toluene were then measured over Ru-$ZnIn_2S_4$ catalysts. When toluene and toluene-d_8 were equivalently mixed and subjected to reaction, KIE based on the amount of hydrogen and deuterium atoms at the benzyl sites of bibenzyl was calculated to be 7.7 ± 0.2 (Supplementary Table 7). The primary KIE coincides with a C–H bond-breaking event contributing to the rate-limiting step[45].

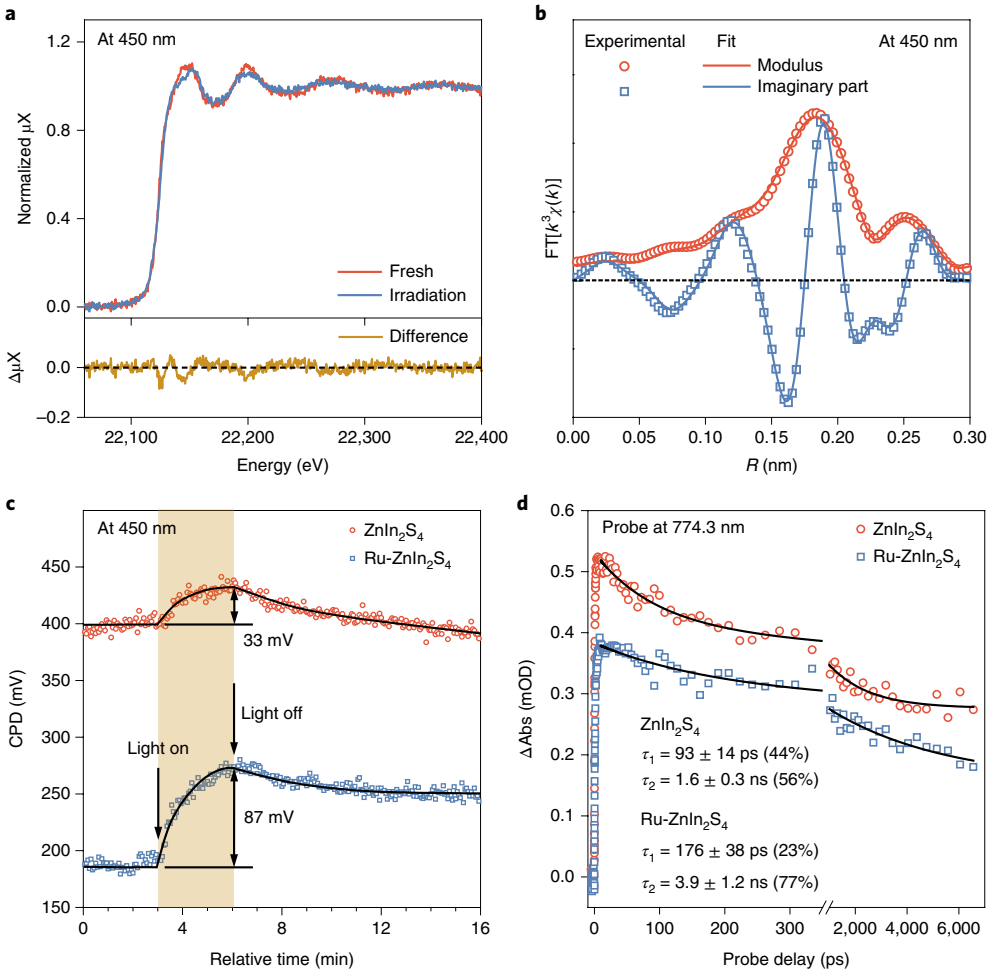

Fig. 5 | Operando and photophysical characterization of the Ru-$ZnIn_2S_4$ photocatalyst. a,**b**, Operando XANES spectra (**a**) and fit of the FT k^3-weighted $\chi(k)$ (**b**) of the EXAFS signals of Ru-$ZnIn_2S_4$ at the Ru K edge. **c**, CPD of $ZnIn_2S_4$ and Ru-$ZnIn_2S_4$. **d**, Transient absorption kinetics recorded by analysing absorption at 774.3 nm for $ZnIn_2S_4$ and Ru-$ZnIn_2S_4$. During operando XANES/EXAFS experiments and CPD, the photocatalyst was irradiated with a 450 nm laser; during transient absorption kinetics it was excited with a 400 nm laser. Errors in transient absorption kinetics represent the standard deviation of the mean for lifetimes, and the values in parentheses are the relative amplitudes of the corresponding lifetime components. Curves drawn on top of CPD data are guides to the eye. mOD, milli-optical density.

Similar to toluene, dehydrocoupling of 2,5-DMF starts with oxidizing the furfuryl C–H bond by photogenerated holes. Before C–C coupling, part of the furfuryl radicals migrates to furan rings due to resonance[46], thus giving a variety of isomer products. It is likely that secondary-carbon radicals of $\mathbf{C_{12}}$-**2** have larger steric hindrance than the primary-carbon radicals, and thus have long enough lifetimes to migrate to furan rings and afford $\mathbf{C_{18}}$-**4** rather than $\mathbf{C_{18}}$-**3** (see Supplementary Table 3 for their molecular structures) as the predominant trimer.

The proposed reaction mechanism of visible-light-driven dehydrocoupling of 2,5-DMF is shown in Fig. 4c. The n-type Ru-$ZnIn_2S_4$ semiconductor has a valence band (VB) top potential of 1.49 V (versus reversible hydrogen electrode (RHE), Supplementary Fig. 16), larger than the oxidation potential of 2,5-DMF (Supplementary Fig. 17), thus justifying that the photogenerated holes of Ru-$ZnIn_2S_4$ are oxidizing the substrate. After excitation by visible light, photogenerated holes oxidize the furfuryl C–H bond of 2,5-DMF, affording furfuryl radicals and protons. The furfuryl radicals undergo resonance, and after C–C coupling, form dimeric isomers. Dimers react with 2,5-DMF or themselves, yielding trimers and tetramers as the DFP constituents. Meanwhile, the generated protons interact with photogenerated electrons in the conduction band (CB, −0.85 V versus RHE) and are reduced to H_2.

Studies of Ru-$ZnIn_2S_4$ by operando XANES/EXAFS

The Ru-$ZnIn_2S_4$ catalyst was studied by operando XANES/EXAFS, by suspending the catalyst in 2,5-DMF/CH_3CN solution and irradiating with a 450 nm laser diode. The results showed that the most significant modifications take place at the Ru edge (Fig. 5a and Supplementary Fig. 18): the XANES/EXAFS results evolve during the first 2 h of irradiation and are constant after that time. The XANES spectrum of this sample can be reasonably fitted by a combination of the spectrum from Ru metal and Ru-$ZnIn_2S_4$ fresh material with a 22% contribution from the Ru metal, indicating that Ru is partially reduced to metallic Ru by photogenerated electrons. In agreement with this, the fit of the EXAFS spectrum (Fig. 5b and Supplementary Table 8) revealed an increase in the CN of Ru–Ru to 2.0 and a decrease of the CN to 4.4 in the Ru–S shell. This can be rationalized by considering that as Ru is reduced and exposed on the surface, forming very small metal clusters, metal atoms from the clusters have a very low Ru–S CN because interaction between Ru and sulfur ions is present only at the interface between the

metal clusters and the support. Therefore, as the contribution of Ru clusters increases, the Ru–S mean CN decreases. The reduction of substitutional Ru ions can be reasonably linked to the deactivation observed during the first 2 h of irradiation, suggesting that Ru clusters are marginally involved in the C–H activation and in coupling of the formed radicals, but we cannot exclude that they are involved in the H_2 evolution steps. The above results also imply that Ru ions hosted in the $ZnIn_2S_4$ matrix indeed promote the photocatalytic activity of $ZnIn_2S_4$ in dehydrocoupling reactions, because depletion of these species corresponds to a partial loss of catalytic activity of the photocatalyst. Notably, the XANES signals at Zn and In K edges are only marginally affected by irradiation (Supplementary Fig. 19) and no significant modifications were observed by analysis of Zn and In EXAFS signals (Supplementary Table 8).

Ru dopants in improving charge separation efficiency

Doping Ru into a $ZnIn_2S_4$ lattice results in the bandgap narrowing from 2.45 to 2.34 eV and the absorption tail rising up to 800 nm (Supplementary Fig. 20a); this is derived from destruction of the long-range order of the atomic structure by Ru dopants in the lattice[47]. Following irradiation at 450 nm, the increase in surface potentials is ascribed to photogenerated holes transferring from the bulk to the surface (Fig. 5c)[48,49]. A variation in the contact potential difference ($CPD_{light} - CPD_{dark}$) of 87 mV was obtained for Ru-$ZnIn_2S_4$, which is higher than that of pristine $ZnIn_2S_4$ (33 mV). The higher surface potential variation of Ru-$ZnIn_2S_4$ can be ascribed to the promotion of charge separation efficiency, which leads to a larger photovoltage. Furthermore, the CPD signal decay of Ru-$ZnIn_2S_4$ became slower than that of pristine $ZnIn_2S_4$ when turning off the light. Both results agree with suppressed hole–electron recombination[36]. In line with this, the photoluminescence spectrum of Ru-$ZnIn_2S_4$ shows decreased intensity relative to $ZnIn_2S_4$ (Supplementary Fig. 20b). Ru dopants also prolong the lifetimes of charge carriers, as proved by transient absorption kinetics (Fig. 5d). The positive signals of $ZnIn_2S_4$ and Ru-$ZnIn_2S_4$ probed at 774.3 nm represent electrons in an excitation state[50]. The signals were bi-exponentially fitted and two distinct lifetimes were obtained[7]. Doping Ru into $ZnIn_2S_4$ improves both the short- and long-lived lifetimes (τ_1 from 93 ± 14 to 176 ± 38 ps; τ_2 from 1.6 ± 0.3 to 3.9 ± 1.2 ns), presumably due to improved density of defects caused by Ru-induced destruction of the long-range order of the $ZnIn_2S_4$ matrix. The long-lived charge carrier lifetime can be attributed to slow electron–hole recombination when the holes are trapped at defects (Supplementary Fig. 21)[36]. In agreement with this, the relative amplitude of the long-lived lifetime increases from 56% to 77%. The consistency of the improved charge separation efficiency and AQY confirms the role of Ru ions substituted in the positions of indium ions in promoting the reactivity of the $ZnIn_2S_4$ catalyst.

Conclusions

This work presents the conversion of lignocellulose-derived 2,5-DMF and 2-MF to H_2 and DFPs through dehydrogenative C–C coupling using visible light over a Ru-doped $ZnIn_2S_4$ catalyst with AQY up to 15.2%. Photogenerated holes oxidize the furfuryl C–H bond of 2,5-DMF/2-MF, delivering protons and furfuryl radicals that, through C–C coupling, form the desired DFPs. Meanwhile, the protons are reduced to H_2 by concomitantly generated electrons. After HDO reaction, the DFPs are converted into ~C_{10}–C_{18} alkanes consisting of straight- and branched-chain alkanes, making the diesel fuels comparable to petroleum diesel in terms of alkane constituents. Moreover, feedstocks derived from hexosan and pentosan are readily converted into H_2 and DFPs over the Ru-$ZnIn_2S_4$ photocatalyst. Ru ions hosted in the $ZnIn_2S_4$ matrix improve light harvesting and charge separation efficiency, thereby facilitating C–H activation for the coproduction of H_2 and DFPs. Future works should focus on improving the yields of C–C coupling products with respect to other thermocatalytic processes or chemical synthesis by the development of more efficient catalysts to further improve the AQYs of dehydrocoupling reactions.

Methods

Reagents. $ZnSO_4{\cdot}7H_2O$ (99.5%), $InCl_3{\cdot}4H_2O$ (99.9%), thioacetamide (TAA, 99%), cetyl trimethyl ammonium bromide (CTAB), 2,5-dimethylfuran (2.5-DMF, 99%) and 2-MF (98%) were purchased from Shanghai Aladdin Bio-Chem Technology Co. $RuCl_3{\cdot}xH_2O$ (99.9% metal basis with a Ru content of 36–38%) was purchased from Shenyang Research Institute of Refractory. $NbCl_5$ (99+% based on Nb) was purchased from Strem Chemicals. $(NH_3)_4Pd(NO_3)_2$ (98%) was purchased from Shanghai Makclin Biochemical Co. 2,5-DMF and 2-MF were redistilled before use; other reagents were used as received without further purification.

Preparation of pristine $ZnIn_2S_4$ catalyst. $ZnIn_2S_4$ was prepared according to a literature procedure[51]. Briefly, $ZnSO_4{\cdot}7H_2O$ (294.0 mg), $InCl_3{\cdot}4H_2O$ (624.2 mg) and CTAB (260.6 mg) were dissolved in 20 ml of MilliQ water in a 100 ml beaker and magnetically stirred for 30 min at room temperature followed by the addition of TAA (604.8 mg) into the solution. After being stirred for another 30 min, the mixture was transferred to a 50 ml stainless Teflon-lined autoclave, tightly sealed and heated at 160 °C for 20 h. The autoclave was then naturally cooled to room temperature. Caution: toxic H_2S gas is generated. After being washed with absolute ethanol (4 × 25 ml) and MilliQ water (2 × 25 ml), a yellow solid was obtained after being dried in vacuum at 60 °C for 12 h. The yield was more than 95%.

Preparation of Ru-$ZnIn_2S_4$. Ru-doped $ZnIn_2S_4$ was prepared by a hydrothermal method. Briefly, $ZnSO_4{\cdot}7H_2O$ (294.0 mg), $InCl_3{\cdot}4H_2O$ (624.2 mg) and CTAB (260.6 mg) were dissolved in 20 ml of MilliQ water in a 100 ml beaker and magnetically stirred, followed by the addition of $RuCl_3$ aqueous solution (384 µl, 13.86 mmol l^{-1}) dropwise. After stirring for 30 min at room temperature, TAA (604.8 mg) was added into the solution, which was stirred for another 30 min. The mixture was transferred to a 50 ml stainless Teflon-lined autoclave, tightly sealed and heated at 160 °C for 20 h. The autoclave was cooled to room temperature naturally after the reaction. Caution: toxic H_2S gas is generated. After being washed with absolute ethanol (4 × 25 ml) and MilliQ water (2 × 25 ml), a dark yellow solid was obtained after being dried in vacuum at 60 °C for 12 h. The yield was more than 95%.

Preparation of Pd/Nb_2O_5. Nb_2O_5 was prepared by a solvothermal method according to the literature[52]. Briefly, 10 mmol of $NbCl_5$ was dissolved in 80 ml of absolute ethanol ($NbCl_5$/ethanol solution) by ultrasonication. Into another flask was added 2.0 g of CTAB, followed by 30 ml of absolute ethanol. Once the CTAB had totally dissolved under stirring, the prepared $NbCl_5$/ethanol solution was added dropwise over 10 min. The system was kept stirring at 35 °C for 1 h before being transferred to a Teflon-lined autoclave and heated at 160 °C for 24 h. After reaction, the system was cooled to room temperature naturally and washed with absolute ethanol (3 × 25 ml) followed by MilliQ water (3 × 25 ml); a light grey solid was obtained after being dried in vacuum at 60 °C for 12 h. The crude Nb_2O_5 was calcined at 500 °C for 5 h (ramp rate of 2 °C min^{-1}) to yield the Nb_2O_5 material.

Pd/Nb_2O_5 with a Pd loading of 2.0 wt% was prepared by an impregnation method. Briefly, 500 mg of the prepared Nb_2O_5 was dispersed in 20 ml of MilliQ water with stirring, into which was added $(NH_3)_4Pd(NO_3)_2$ aqueous solution (8.642 mmol l^{-1}, 10.4 ml). The system was stirred for 4 h before rotary evaporation at 65 °C, and then dried at 100 °C for 2 h. The orange Pd/Nb_2O_5 solid was obtained after calcination at 500 °C for 3 h (ramp rate of 10 °C min^{-1}).

Photocatalytic coproduction of H_2 and DFPs. Photocatalytic reactions were conducted in a home-made quartz photoreactor equipped with blue light-emitting diodes (LEDs; emission at 455 nm)[53]. Briefly, photocatalyst, methylfurans and CH_3CN were added into the reaction tubes, before replacing the atmosphere with Ar. The reaction tubes were irradiated for a desired reaction time under stirring. The autogenous temperature, measured by thermocouple, was ~42 °C. Caution: protection by wearing eye goggles to shield 455 nm light is mandatory to avoid injuring the eyes.

Standard reaction conditions: 10 mg of catalyst, substrate (0.5 ml of 2,5-DMF or 0.5 ml of 2-MF or a mixture of 0.25 ml of 2,5-DMF + 0.75 ml of 2-MF), 0.5 ml of CH_3CN, Ar atmosphere, 9 W blue LEDs (455 nm), irradiation for 12 h.

Catalyst lifetime evaluation conditions: 200 mg of Ru-$ZnIn_2S_4$, 25 ml of 2,5-DMF, 25 ml of CH_3CN, Ar atmosphere, 86 W blue LEDs, irradiation for 100 h.

Scaled-up reaction conditions: 200 mg of Ru-$ZnIn_2S_4$, 5 ml of 2,5-DMF + 15 ml of 2-MF, 10 ml of CH_3CN, Ar atmosphere, 86 W blue LEDs, irradiation for 48 h.

Thermocatalytic HDO of DFPs. Before the HDO reactions, the photocatalytic reaction products underwent centrifugation at 10,000 r.p.m. min^{-1}, filtration through a 0.22 µm nylon syringe filter, rotary evaporation at 40 °C and finally purification by column chromatography (CH_2Cl_2, petroleum ether = 1:20) to totally remove the Ru-$ZnIn_2S_4$ catalyst, unreacted substrate and CH_3CN. For HDO reactions, 20 mg of Pd/Nb_2O_5, 0.02 mmol of $Yb(CF_3SO_3)_3$, 50 mg of the pretreated DFPs and 3.0 ml of *n*-tetradecane/cyclohexane solution (internal standard) were

added into a Teflon-lined reaction autoclave. Thereafter, the reaction system was filled with 3.0 MPa of H_2 then maintained at 120 and 210 °C for a period, successively.

Qualitative analysis of the components of DFPs. The molecular structures of the diesel fuel components were deduced according to the produced alkanes because the selectivity of dealkylation and isomerization is below 3% according to Supplementary Table 3. The diesel fuel components were qualitatively analysed by gas chromatography–mass spectrometry (GC-MS, Agilent 5975C with a triple-axis detector) based on the characteristic fragment ion peaks (FIPs) in a mass spectrogram. A detailed description of the analytic methods, deduced structures of the diesel fuel components and corresponding NMR/MS spectra are provided in Supplementary Notes 1 and 2, Supplementary Tables 3 and 4 and Supplementary Figs. 22–57, respectively.

Quantitative analysis of H_2. H_2 was quantified with He as the internal standard. After the reactions, He was injected into the reaction systems, mixed well, then followed by analysis by GC equipped with a thermal conductivity detector (GC-TCD, Techcomp 7900) with Ar as the carrier gas. Supplementary Fig. 58a shows the calibration curves of H_2 and He, respectively, together with fitting lines. The produced H_2 can be calculated by the following equation:

$$n(\mathrm{H_2}) = \frac{0.561 \times I(\mathrm{H_2}) \times V(\mathrm{He})/\mathrm{ml}}{1.137 \times I(\mathrm{He})} \times \frac{101.3}{8.314 \times 298}\mathrm{mmol} = 0.0202 \times \frac{I(\mathrm{H_2})}{I(\mathrm{He})} \times \frac{V(\mathrm{He})}{\mathrm{ml}}\mathrm{mmol} \quad (1)$$

where $n(H_2)$ is the H_2 produced in the reaction system (mmol), $I(H_2)$ and I(He) are the TCD responses of H_2 and He, respectively, and V(He) is the volume of He injected into the reaction system. The produced H_2 is expressed as $n(H_2)/m_{catalyst}$, where $m_{catalyst}$ is the mass of the catalyst.

Quantitative analysis of DFPs. DFPs were quantified with mesitylene as the internal standard. After analysing H_2, mesitylene was added into the reaction system, which was mixed well. The mixture was filtered through a 0.22 μm nylon syringe filter and analysed by GC equipped with flame ionization detector (GC-FID, Agilent 7890A). Assuming relative responsive factors $g_{trimers} = \frac{2}{3} \times g_{dimers}$ and $g_{tetramers} = \frac{2}{4} \times g_{dimers}$, the productivities of the products and selectivity of DFPs and branched-chain DFPs were calculated using the following equations:

$$f_{C_{12}-2} = \frac{m_{C_{12}-2}/A_{C_{12}-2}}{m_{mesitylene}/A_{mesitylene}} \quad (2)$$

$$g_{dimers} = g_{C_{12}-2} = \frac{f_{C_{12}-2}}{M_{C_{12}-2}/M_{mesitylene}} \quad (3)$$

$$\text{Productivity of product} = \frac{g_{product}}{g_{dimers}} \times \frac{M_{product}}{M_{C_{12}-2}} \times f_{C_{12}-2} \times m_{mesitylene} \times \frac{A_{product}}{m_{mesitylene}} / m_{catalyst} \quad (4)$$

$$\text{Selectivity of DFPs} = \frac{g_{dimers} \times A_{dimers} + g_{trimers} \times A_{trimers}}{g_{dimers} \times A_{dimers} + g_{trimers} \times A_{trimers} + g_{tetramers} \times A_{tetramers}} \times 100\% \quad (5)$$

$$\text{Selectivity of branched-chain DFPs} = \frac{g_{dimers} \times A_{dimers,B} + g_{trimers} \times A_{trimers,B}}{g_{dimers} \times A_{dimers} + g_{trimers} \times A_{trimers} + g_{tetramers} \times A_{tetramers}} \times 100 \quad (6)$$

where g_{dimers}, $g_{trimers}$, $g_{tetramers}$ and $g_{C_{12}-2}$ are the relative responsive factors of dimers, trimers, tetramers and **C_{12}-2**, respectively; $f_{C_{12}-2}$ is the relative mass calibration factor (RMCF) of **C_{12}-2**; $m_{C_{12}-2}$, $m_{mesitylene}$ and $m_{catalyst}$ are the mass of **C_{12}-2**, mesitylene and the catalyst, respectively; $M_{C_{12}-2}$, $M_{mesitylene}$ and $M_{product}$ are the molecular weights (M_w) of **C_{12}-2**, mesitylene and product, respectively; $A_{C_{12}-2}$, $A_{mesitylene}$, $A_{product}$, A_{dimers}, $A_{trimers}$, $A_{tetramers}$, $A_{dimers,B}$ and $A_{trimers,B}$ are the GC area of **C_{12}-2**, mesitylene, product, dimers, trimers, tetramers, branched-chain dimers and branched-chain trimers, respectively. In the calculation of the selectivity of branched-chain DFPs in the case of the 2-MF substrate, the branched-chain tetramers were also included. $f_{C_{12}-2}$ was experimentally determined with isolated **C_{12}-2** (Supplementary Figs. 22 and 58b).

Quantitative analysis of diesel fuels. After HDO reaction, the mixture was filtered through a 0.22 μm nylon syringe filter and analysed by GC-FID. The RMCFs of *n*-undecane, *n*-dodecane and *n*-octadecane are very similar, with *n*-tetradecane as the internal standard (Supplementary Fig. 58c–e), so the RMCF of *n*-octadecane was used to quantify the C_{15}–C_{18} alkanes. The yields of C_n alkane were calculated with the following equations:

$$f_{C_n} = \frac{m_{C_n}/A_{C_n}}{m_{n-\text{tetradecane}}/A_{n-\text{tetradecane}}} \quad (7)$$

$$\text{Yield of } C_n = \frac{(f_{C_n} \times m_{n-\text{tetradecane}} \times A_{C_n}/A_{n-\text{tetradecane}})/M_{C_n}}{m_{DFPs}/M_{ave}} \times 100\% \quad (8)$$

where f_{C_n} is the RMCF of the corresponding alkane; m_{C_n}, $m_{n-\text{tetradecane}}$ and m_{DFPs} are the mass of C_n alkane, *n*-tetradecane and DFPs, respectively; A_{C_n} and $A_{n-\text{tetradecane}}$ are the GC area of C_n alkane and *n*-tetradecane, respectively; M_{C_n} is the M_w of C_n alkane and M_{ave} is the mean M_w of the DFPs.

AQY measurements. The AQYs of the photocatalytic dehydrocoupling of 2,5-DMF, 2-MF and their mixture were measured over Ru-$ZnIn_2S_4$ and $ZnIn_2S_4$ with blue LEDs (input power of 27.2 W, 452 ± 10 nm) by top irradiation. The number of photons reaching the top of the reaction solution was measured with a calibrated Si photodiode (LS-100, EKO Instruments). The AQYs (η) for the formation of DFPs were calculated using the following equation:

$$\eta = \frac{2n_{dimers}\ (\mathrm{mol}) \times N_A\ (\mathrm{mol^{-1}}) + 4n_{trimers}\,(\mathrm{mol}) \times N_A(\mathrm{mol^{-1}}) + 6n_{tetramers}\,(\mathrm{mol}) \times N_A(\mathrm{mol^{-1}})}{I\,(\mathrm{cm^{-2}\,s^{-1}}) \times t\,(\mathrm{s}) \times S(\mathrm{cm^2})} \times 100\% \quad (9)$$

where n_{dimers}, $n_{trimers}$ and $n_{tetramers}$ are the formed dimers, trimers and tetramers, respectively, and N_A, I, t and S represent Avogadro's constant, light intensity, reaction time and irradiation area, respectively.

Mechanistic studies using toluene as a model compound. The radical mechanism of the dehydrocoupling reaction has been demonstrated by studying the products of a radical trapping experiment performed with the following conditions: 1.0 ml of toluene, 31 mg of TEMPO (0.2 mmol), 10 mg of Ru-$ZnIn_2S_4$, Ar atmosphere, 9 W blue LEDs (455 nm), irradiation for 12 h. The products were determined by GC-MS analysis. In the cross-coupling experiments, a mixture of 0.5 ml of *p*-xylene + 0.5 ml of *p*-methyl anisole was used as the substrate instead of toluene.

Powder XRD patterns. XRD patterns were collected with a PANalytical X-Pert PRO diffractometer, using Cu-Kα radiation at 40 kV and 20 mA. Continuous scans were collected in a 2θ range of 10–80°.

TEM. Samples for TEM were prepared by dispersing catalyst in ethanol and sonication for 20 min. The suspension (15 μl) was loaded onto a Cu TEM grid and dried. TEM images were obtained using a JEOL JEM-2100.

X-ray absorption spectroscopy. X-ray absorption spectra (named here μX both for normalized linear absorption coefficient or fluorescence yield), in the near edge (XANES) and extended (EXAFS) energy ranges, were measured at the SAMBA beamline[54] of Synchrotron SOLEIL; spectra at the Ru K edge were collected by measuring the K_α emission of Ru with a four-diode Si drift detector Vortex ME4 from Hitachi. Dead time correction was applied on the basis of the calibrated estimate from DxpMap DSP cards by XIA Ltd. In and Zn data were measured in transmission and fluorescence mode; the transmission mode was preferred for data analysis. EXAFS data analysis was carried out with theoretical standards from Feff 8.4[55] and with the software Horae[56] for data handling and fitting. All fits were carried out in R-space ($3 \le k \le 10$ Å^{-1}; $1 \le r \le 3$ Å; EXAFS data have been k^1 weighted). The amplitude reduction factor (S_0^2) was estimated by fitting the EXAFS signal of finely meshed Ru metallic powders and its value was fixed to 0.87(5). Similarly, it was found to be 0.9 for Zn and In K edges.

Ex situ samples were analysed after deposition of the powders on polyvinylidene fluoride (PVDF) membrane. Operando spectra were acquired using conditions very similar to those used for the photocatalytic tests. Briefly, 10 mg of the Ru-$ZnIn_2S_4$ photocatalyst was suspended in 0.5 ml of 2,5-DMF and 0.5 ml of CH_3CN within a vial transparent to X-ray and visible light and closed with a Teflon/silicone septum (quartz vial with 0.5 mm wall for Ru and In K edges and polystyrene vial for Zn K edge). After removal of air by an Ar stream, the vial was placed in the X-ray path of the SAMBA beamline and maintained under stirring

during acquisition of spectra. During operando experiments, the photocatalyst was irradiated with a 450 nm diode emission laser, with an irradiation power of 100 mW cm^{-2} over a spot with a diameter of 0.5 cm^2. Irradiation was performed for 7.5 h, during which acquisition of EXAFS spectra was performed every 5 min.

CPD. CPD was recorded using a Kelvin probe force microscope (KPFM). The fluorine-doped tin oxide (FTO) glasses (resistivity, 0.01 Ω cm) were cleaned according to the literature[48]. Briefly, the original FTO glasses were cleaned with acetone (30 min), ethanol (30 min) and H_2O (30 min) by ultrasonics. A suspension of $ZnIn_2S_4$ or Ru-$ZnIn_2S_4$ in ethanol, obtained by ultrasonication for 5 h, was then added dropwise (five drops; each drop of suspension was added after the ethanol of the previous one had dried). Before KPFM measurements, the FTO glasses were treated in vacuum at 150 °C for 2 h. KPFM and atomic force microscopy images were taken on a Bruker Dimension V SPM system equipped with Pt/Ir coated tips (resonant frequency 72 kHz). Images were acquired at scan rates of 0.5 Hz and the tip lift height was set to100 nm in the tapping mode for potential mapping. The irradiation wavelength was 450 nm. CPD is defined as the difference between the work functions of the tip and sample.

Ultrafast transient absorption spectroscopy. The femtosecond transient absorption set-up used for this study was based on a regenerative amplified Ti:sapphire laser system from Coherent (800 nm, 35 fs, 6 mJ per pulse and 1 kHz repetition rate), nonlinear frequency mixing techniques and a Femto-TA100 spectrometer (Time-Tech Spectra). Briefly, the 800 nm output pulse from the regenerative amplifier was split into two parts with a 50% beamsplitter. The transmitted part was used to pump a TOPAS optical parametric amplifier, which generated a wavelength-tunable laser pulse from 250 nm to 2.5 μm. A 400 nm laser was used as the pump beam. The reflected 800 nm beam was split again into two parts. One part, less than 10%, was attenuated with a neutral density filter and focused into a 3 mm TiO_2 window to generate a white light continuum from 430 nm to 800 nm for use as a probe beam. The probe beam was focused with an Al parabolic reflector onto the sample. After the sample, the probe beam was collimated and then focused into a fibre-coupled spectrometer with CMOS sensors and detected at a frequency of 1 kHz. The intensity of the pump pulse used in the experiment was controlled by a variable neutral-density filter wheel and kept at 70 μJ cm^{-2}. The delay between the pump and probe pulses was controlled by a motorized delay stage. The pump pulses were chopped by a synchronized chopper at 500 Hz and the absorbance change was calculated with two adjacent probe pulses (pump-blocked and pump-unblocked). All experiments were performed at room temperature. The sample for measurement was dispersed in ethanol and held in a 2 mm quartz curvette after centrifugation at 2,000 r.p.m. for 10 min to remove the unstable suspension.

Data availability

Additional and supporting data are provided in the Supplementary Information. Further data that support the plots within this Article and other findings of this study are available from the corresponding author upon reasonable request.

Received: 16 July 2018; Accepted: 29 April 2019;
Published online: 10 June 2019

References

1. Shih, C. F., Zhang, T., Li, J. & Bai, C. Powering the future with liquid sunshine. *Joule* **2**, 1925–1949 (2018).
2. Li, X. B. et al. Self-assembled framework enhances electronic communication of ultrasmall-sized nanoparticles for exceptional solar hydrogen evolution. *J. Am. Chem. Soc.* **139**, 4789–4796 (2017).
3. Selcuk, S. & Selloni, A. Facet-dependent trapping and dynamics of excess electrons at anatase TiO_2 surfaces and aqueous interfaces. *Nat. Mater.* **15**, 1107–1112 (2016).
4. Han, G. et al. Visible-light-driven valorization of biomass intermediates integrated with H_2 production catalyzed by ultrathin Ni/CdS nanosheets. *J. Am. Chem. Soc.* **139**, 15584–15587 (2017).
5. Shi, R. et al. Interstitial P-doped CdS with long-lived photogenerated electrons for photocatalytic water splitting without sacrificial agents. *Adv. Mater.* **30**, 1705941 (2018).
6. Shown, I. et al. Carbon-doped SnS_2 nanostructure as a high-efficiency solar fuel catalyst under visible light. *Nat. Commun.* **9**, 169 (2018).
7. Yang, W. et al. Enhanced photoexcited carrier separation in oxygen-doped $ZnIn_2S_4$ nanosheets for hydrogen evolution. *Angew. Chem. Int. Ed.* **55**, 6716–6720 (2016).
8. Luo, N. et al. Photocatalytic oxidation–hydrogenolysis of lignin β-O-4 models via a dual light wavelength switching strategy. *ACS Catal.* **6**, 7716–7721 (2016).
9. Guo, M., Song, W. & Buhain, J. Bioenergy and biofuels: history, status and perspective. *Renew. Sust. Energ. Rev.* **42**, 712–725 (2015).
10. Zhang, P. et al. Streamlined hydrogen production from biomass. *Nat. Catal.* **1**, 332–338 (2018).
11. Wakerley, D. W. et al. Solar-driven reforming of lignocellulose to H_2 with a CdS/CdO_x photocatalyst. *Nat. Energy* **2**, 17021 (2017).
12. Kuehnel, M. F. & Reisner, E. Solar hydrogen generation from lignocellulose. *Angew. Chem. Int. Ed.* **57**, 3290–3296 (2018).
13. Latorre-Sanchez, M., Primo, A. & Garcia, H. P-doped graphene obtained by pyrolysis of modified alginate as a photocatalyst for hydrogen generation from water–methanol mixtures. *Angew. Chem. Int. Ed.* **52**, 11813–11816 (2013).
14. Karp, E. M. et al. Renewable acrylonitrile production. *Science* **358**, 1307–1310 (2017).
15. Zhou, Z.-z, Liu, M. & Li, C.-J. Selective copper–N-heterocyclic carbene (copper-NHC)-catalyzed aerobic oxidative cleavage of β-1 lignin models to aldehydes. *ACS Catal.* **7**, 3344–3348 (2017).
16. Bond, J. Q. et al. Production of renewable jet fuel range alkanes and commodity chemicals from integrated catalytic processing of biomass. *Energy Environ. Sci.* **7**, 1500–1523 (2014).
17. Via, L. D., Recchi, C., Davies, T. E., Greeves, N. & Lopez-Sanchez, J. A. Visible-light-controlled oxidation of glucose using titania-supported silver photocatalysts. *ChemCatChem* **8**, 3475–3483 (2016).
18. Xie, S. et al. Visible light-driven C–H activation and C–C coupling of methanol into ethylene glycol. *Nat. Commun.* **9**, 1181 (2018).
19. Deneyer, A. et al. Direct upstream integration of biogasoline production into current light straight run naphtha petrorefinery processes. *Nat. Energy* **3**, 969–977 (2018).
20. de Beeck, B. O. et al. Direct catalytic conversion of cellulose to liquid straight-chain alkanes. *Energy Environ. Sci.* **8**, 230–240 (2015).
21. Climent, M. J., Corma, A. & Iborra, S. Conversion of biomass platform molecules into fuel additives and liquid hydrocarbon fuels. *Green Chem.* **16**, 516–547 (2014).
22. Shylesh, S., Gokhale, A. A., Ho, C. R. & Bell, A. T. Novel strategies for the production of fuels, lubricants and chemicals from biomass. *Acc. Chem. Res.* **50**, 2589–2597 (2017).
23. Zhu, Y. et al. Efficient synthesis of 2,5-dihydroxymethylfuran and 2,5-dimethylfuran from 5-hydroxymethylfurfural using mineral-derived Cu catalysts as versatile catalysts. *Catal. Sci. Technol.* **5**, 4208–4217 (2015).
24. Yang, X. et al. Efficient synthesis of furfuryl alcohol and 2-methylfuran from furfural over mineral-derived Cu/ZnO catalysts. *ChemCatChem* **9**, 3023–3030 (2017).
25. Chatterjee, M., Ishizaka, T. & Kawanami, H. Hydrogenation of 5-hydroxymethylfurfural in supercritical carbon dioxide–water: a tunable approach to dimethylfuran selectivity. *Green Chem.* **16**, 1543–1551 (2014).
26. Thananatthanachon, T. & Rauchfuss, T. B. Efficient production of the liquid fuel 2,5-dimethylfuran from fructose using formic acid as a reagent. *Angew. Chem. Int. Ed.* **49**, 6616–6618 (2010).
27. Guo, W. et al. Efficient hydrogenolysis of 5-hydroxymethylfurfural to 2,5-dimethylfuran over a cobalt and copper bimetallic catalyst on N-graphene-modified Al_2O_3. *Green Chem.* **18**, 6222–6228 (2016).
28. Win, D. T. Furfural-gold from garbage. *AU J. Technol.* **8**, 185–190 (2005).
29. Lange, J. P., van der Heide, E., van Buijtenen, J. & Price, R. Furfural—a promising platform for lignocellulosic biofuels. *ChemSusChem* **5**, 150–166 (2012).
30. Li, G. et al. Synthesis of high-quality diesel with furfural and 2-methylfuran from hemicellulose. *ChemSusChem* **5**, 1958–1966 (2012).
31. Corma, A., de la Torre, O. & Renz, M. Production of high quality diesel from cellulose and hemicellulose by the Sylvan process: catalysts and process variables. *Energy Environ. Sci.* **5**, 6328–6344 (2012).
32. Huber, G. W., Chheda, J. N., Barrett, C. J. & Dumesic, J. A. Production of liquid alkanes by aqueous-phase processing of biomass-derived carbohydrates. *Science* **308**, 1446–1450 (2005).
33. Gumidyala, A., Wang, B. & Crossley, S. Direct carbon–carbon coupling of furanics with acetic acid over Bronsted zeolites. *Sci. Adv.* **2**, e1601072 (2016).
34. Bond, J. Q., Alonso, D. M., Wang, D., West, R. M. & Dumesic, J. A. Integrated catalytic conversion of gamma-valerolactone to liquid alkenes for transportation fuels. *Science* **327**, 1110–1113 (2010).
35. Balakrishnan, M., Sacia, E. R. & Bell, A. T. Syntheses of biodiesel precursors: sulfonic acid catalysts for condensation of biomass-derived platform molecules. *ChemSusChem* **7**, 1078–1085 (2014).
36. Jiao, X. et al. Defect-mediated electron-hole separation in one-unit-cell $ZnIn_2S_4$ layers for boosted solar-driven CO_2 reduction. *J. Am. Chem. Soc.* **139**, 7586–7594 (2017).
37. Yang, Y., Sun, C., Ren, Y., Hao, S. & Jiang, D. New route toward building active ruthenium nanoparticles on ordered mesoporous carbons with extremely high stability. *Sci. Rep.* **4**, 4540 (2014).
38. Ohba, T. et al. EXAFS studies of Pd nanoparticles: direct evidence for unusual Pd–Pd bond elongation. *Chem. Lett.* **44**, 803–805 (2015).
39. Niu, L. et al. Photo-induced oxidant-free oxidative C–H/N–H cross-coupling between arenes and azoles. *Nat. Commun.* **8**, 14226 (2017).
40. Meng, L. et al. Gold plasmon-induced photocatalytic dehydrogenative coupling of methane to ethane on polar oxide surfaces. *Energy Environ. Sci.* **11**, 294–298 (2018).

41. Dutta, S. & Saha, B. Hydrodeoxygenation of furylmethane oxygenates to jet and diesel range fuels: probing the reaction network with supported palladium catalyst and hafnium triflate promoter. *ACS Catal.* **7**, 5491–5499 (2017).
42. Ji, S., Cao, W., Yu, Y. & Xu, H. Dynamic diselenide bonds: exchange reaction induced by visible light without catalysis. *Angew. Chem. Int. Ed.* **53**, 6781–6785 (2014).
43. Nomura, M., Takayama, C. & Kajitani, M. Electrochemical behavior of nickeladithiolene S,S′-dialkyl adducts: evidence for the formation of a metalladithiolene radical by electrochemical redox reactions. *Inorg. Chem.* **42**, 6441–6446 (2003).
44. Naesborg, L. et al. Direct enantio- and diastereoselective oxidative homocoupling of aldehydes. *Chem. Eur. J.* **24**, 14844–14848 (2018).
45. King, E. R., Hennessy, E. T. & Betley, T. A. Catalytic C–H bond amination from high-spin iron imido complexes. *J. Am. Chem. Soc.* **133**, 4917–4923 (2011).
46. Mironenko, A. V. & Vlachos, D. G. Conjugation-driven 'reverse Marslvan Krevelen'-type radical mechanism for low-temperature C–O bond activation. *J. Am. Chem. Soc.* **138**, 8104–8113 (2016).
47. Kang, Y. et al. Selective breaking of hydrogen bonds of layered carbon nitride for visible light photocatalysis. *Adv. Mater.* **28**, 6471–6477 (2016).
48. Li, H. et al. Construction and nanoscale detection of interfacial charge transfer of elegant Z-scheme WO_3/Au/In_2S_3 nanowire arrays. *Nano Lett.* **16**, 5547–5552 (2016).
49. Zhu, J. et al. Direct imaging of highly anisotropic photogenerated charge separations on different facets of a single $BiVO_4$ photocatalyst. *Angew. Chem. Int. Ed.* **54**, 9111–9114 (2015).
50. Huang, X. et al. Efficient plasmon-hot electron conversion in Ag-$CsPbBr_3$ hybrid nanocrystals. *Nat. Commun.* **10**, 1163 (2019).
51. Gou, X. et al. Shape-controlled synthesis of ternary chalcogenide $ZnIn_2S_4$ and $CuIn(S,Se)_2$ nano-/microstructures via facile solution route. *J. Am. Chem. Soc.* **128**, 7222–7229 (2006).
52. Xia, Q.-N. et al. Pd/$NbOPO_4$ multifunctional catalyst for the direct production of liquid alkanes from aldol adducts of furans. *Angew. Chem. Int. Ed.* **53**, 9755–9760 (2014).
53. Luo, N. et al. Visible-light-driven self-hydrogen transfer hydrogenolysis of lignin models and extracts into phenolic products. *ACS Catal.* **7**, 4571–4580 (2017).
54. Briois, V. et al. SAMBA: The 4–40 keV X-ray absorption spectroscopy beamline at SOLEIL. *UVX* **2010**, 41–47 (2011).
55. Ankudinov, A. L., Ravel, B., Rehr, J. J. & Conradson, S. D. Real-space multiple-scattering calculation and interpretation of X-ray-absorption near-edge structure. *Phys. Rev. B* **58**, 7565–7576 (1998).
56. Ravel, B. & Newville, M. ATHENA, ARTEMIS, HEPHAESTUS: data analysis for X-ray absorption spectroscopy using IFEFFIT. *J. Synchrotron Radiat.* **12**, 537–541 (2005).

Acknowledgements

The authors acknowledge SOLEIL for provision of synchrotron radiation facilities and thank G. Alizon for technical assistance in using beamline SAMBA. The authors also acknowledge financial support from the National Natural Science Foundation of China (21721004, 21690082, 21690084, 21690080), the Strategic Priority Research Program of Chinese Academy of Sciences (XDB17020300, XDB17000000), the National Natural Science Foundation of China (21711530020), the University of Trieste (programme FRA 2018, project INSIDE), the Italian Ministry for University and Research (MIUR, programme FFABR 2017) and the INSTM consortium.

Author contributions

N.L. and F.W. conceived the research. N.L. conducted most of the experiments in this work, analysed the data and wrote the manuscript. XANES/EXAFS experiments and their discussion were done by T.M., assisted by E.F. T.M., P.F. and E.F. fully revised the manuscript. J.Z. and N.L. designed and fabricated the LED photoreactor. The variation of CPD was measured by W.N., assisted by F.F. J.M.L. carried out the DFT calculations. Transient absorption analysis was done by J.X.L., assisted by S.J. HAADF-STEM and EDX mappings were performed by M.H. Cyclic voltammetry was measured by L.L. Mott–Schottky measurements were done by C.M. T.H. and M.W. added to the discussion and contributed to the preparation of the manuscript. F.W. planned, supervised and led the project.

Competing interests

The authors declare no competing interests.

Additional information

Supplementary information is available for this paper at https://doi.org/10.1038/s41560-019-0403-5.

Reprints and permissions information is available at www.nature.com/reprints.

Correspondence and requests for materials should be addressed to F.W.

Publisher's note: Springer Nature remains neutral with regard to jurisdictional claims in published maps and institutional affiliations.